Long-range transport in asymmetric quadruple quantum dot configurations

David Fernández-Fernández, Johannes C. Bayer, Rolf J. Haug, Gloria Platero

Angaben zur Veröffentlichung / Publication details:

Fernández-Fernández, David, Johannes C. Bayer, Rolf J. Haug, and Gloria Platero. 2025. "Long-range transport in asymmetric quadruple quantum dot configurations." *Communications Physics* 8 (1): 410. https://doi.org/10.1038/s42005-025-02319-3.

communications physics

A Nature Portfolio journal

Article

https://doi.org/10.1038/s42005-025-02319-3

Long-range transport in asymmetric quadruple quantum dot configurations

David Fernández-Fernández [1] ✉, Johannes C. Bayer [2,3], Rolf J. Haug [2] & Gloria Platero [1]

Quantum dot arrays are a versatile platform for investigating coherent charge and spin transport, with direct relevance for scalable quantum information processing. While long-range tunneling has been extensively studied in triple quantum dots, the role of reduced symmetry in quadruple quantum dot (QQD) systems remains largely unexplored. Here we show, employing a master equation approach, that coherent long-range charge transfer can persist in QQDs even under reduced symmetry configurations. We identify clear resonance conditions characterized by strongly suppressed population of the intermediate dots, as well as distinctive signatures such as interference between competing long-range channels and current blockade effects. Our results, obtained with experimentally realistic parameters, establish that efficient long-range transfer does not require perfect symmetry, and provide theoretical guidance for future experimental efforts to harness coherent transport in extended quantum dot arrays for quantum technologies.

Quantum dots (QDs) constitute a highly controllable platform for exploring fundamental quantum phenomena, coherent charge transport, and potential applications in quantum information processing and quantum computing architectures[1,2]. Among various configurations, linear quantum dot arrays have emerged as especially promising, owing to their ability to support long-range coherent charge and spin transport mediated by virtual occupation of intermediate dots, a process known as co-tunneling[3–6].

While spin transport is a key requirement for scaling up spin-based quantum computing architectures, especially for implementing long-distance spin qubit coupling, charge transport remains an essential and experimentally accessible proxy for investigating the underlying coherent tunneling mechanisms that enable such coupling. In particular, charge dynamics directly reflect the structure of the energy spectrum, the strength and symmetry of tunnel couplings, and the role of virtual intermediate states. Studying charge transfer allows us to characterize and isolate regimes where long-range tunneling dominates, including conditions under which occupation of intermediate dots is strongly suppressed.

Substantial insight into coherent transport mechanisms has been obtained from studies on double quantum dot (DQD)[7–12] and triple quantum dot (TQD) systems[13–27]. In DQDs, spin blockade phenomena, arising from Pauli exclusion, have been extensively studied and exploited for spin qubit readout and coherent manipulation[28]. TQD systems have revealed more intricate phenomena, including bipolar spin blockade[29], coherent superpositions avoiding intermediate dots[30], and long-range spin and charge transfer mediated by superexchange interactions[31], where the transfer occurs between not directly coupled QDs. These seminal investigations established the pivotal role of coherent tunneling and spin-dependent interactions in quantum dot arrays.

Extending these concepts to quadruple quantum dot (QQD) systems[32–40] introduces additional complexity and richness due to the increased number of degrees of freedom and an expanded parameter space. As an example, Kondo effect[41] and Nagaoka's ferromagnetism can be observed in QQDs[42]. QQDs have also been proposed as quantum simulators of the Wigner molecule[43], rendering this system particularly interesting for quantum simulation and quantum information applications.

Due to the symmetry of TQD arrays they exhibit perfect dark states, eigenstates with minimal occupation of the intermediate dots, which are crucial for long-range transport[30,31]. In contrast, QQDs lack such internal symmetry[44], and dark states are expected to effectively appear only under highly symmetric configurations. Also, the presence of cross-coupling between the dots in an experimental device can further complicate the emergence of dark states. This difficulty stems from the demanding tuning requirements for multiple parameters, including tunneling amplitudes, inter-dot Coulomb interactions, and gate-defined energy levels. Currently, assisted machine learning techniques are proposed to simplify the tuning of these parameters[45]. However, the existence of long-range transport in reduced symmetric configurations remains an open question.

In this work, we present a theoretical study of charge transport in a linear QQD array coupled to electronic reservoirs where the symmetry requirements are relaxed. Then, we focus on coherent long-range charge transfer under explicitly non-symmetric configurations. Using a master equation formalism in conjunction with an effective co-tunneling

[1]Instituto de Ciencia de Materiales de Madrid ICMM-CSIC, Madrid, Spain. [2]Institut für Festkörperphysik, Leibniz Universität Hannover, Hanover, Germany. [3]Physikalisch-Technische Bundesanstalt, Braunschweig, Germany. ✉e-mail: david.fernandez@csic.es

description, we systematically explore the parameter regimes that enable long-range transport between distant QDs. We identify distinct resonant conditions characterized by suppressed occupation of the intermediate sites. While our study is theoretical, the parameters and conditions considered are compatible with current experimental platforms, and we anticipate our results will inform future experimental efforts[36,37].

Methods

Model for closed system

We aim to study electron spin qubits on GaAs planar QDs, where the spin–orbit interaction is negligible. Furthermore, the main results of this work can be extended to other materials with negligible spin–orbit interaction.

We consider a minimal model comprising Anderson impurities linearly coupled to two fermionic leads, see Fig. 1a, described by the total Hamiltonian $\hat{H} = \hat{H}_0 + \hat{H}_{\text{leads}} + \hat{H}_{\text{coup}}$. The first term describes the quantum dot array populated by electrons, with a single orbital per site. This term is modeled by a Fermi-Hubbard Hamiltonian, given by

$$\begin{aligned}\hat{H}_0 = &\sum_{i=1}^{N=4} \varepsilon_i \hat{n}_i + \sum_{i=1}^{N=4} U_i \hat{n}_{i\uparrow}\hat{n}_{i\downarrow} + \sum_{i\neq j}^{N=4} \frac{V_{i,j}}{2}\hat{n}_i\hat{n}_j \\ &+ \sum_{i=1}^{N-1=3} \sum_{\sigma=\{\uparrow,\downarrow\}} \tau_i \left(\hat{c}^{\dagger}_{i\sigma}\hat{c}_{(i+1)\sigma} + \text{H.c.}\right) \\ &+ \sum_{i=1}^{N=4} \frac{\vec{\Delta}_i}{2}\cdot\vec{\hat{S}}_i,\end{aligned} \tag{1}$$

where ε_i denotes the on-site energy of the i-th dot, U_i is the on-site Coulomb repulsion, $V_{i,j}$ represents the inter-dot Coulomb repulsion, and τ_i is the hopping amplitude between adjacent sites i and $i+1$. The creation (annihilation) operator $\hat{c}^{\dagger}_{i\sigma}$ ($\hat{c}_{i\sigma}$) creates (annihilates) an electron with spin σ at site i, and $\hat{n}_i = \sum_\sigma \hat{n}_{i\sigma}$ is the total occupation operator at site i, with $\hat{n}_{i\sigma} = \hat{c}^{\dagger}_{i\sigma}\hat{c}_{i\sigma}$. Note that no long-range hopping is considered in this model. In GaAs lateral dots, interdot tunneling rates in the range $\tau_i \sim 1 - 10\,\mu$eV are routinely achieved[14,35,37]. These values set the relevant energy and time scales for our simulations. Finally, we include a local Zeeman splitting $\vec{\Delta}_i = g\mu_B \vec{B}_{N,i}$, where μ_B is the Bohr magneton, g is the electron g-factor, $\vec{B}_{N,i}$ is the effective Overhauser magnetic field due to the hyperfine interaction with the nuclei, and g is the electron g-factor. Also, we have defined the spin operators in second quantization as $\vec{\hat{S}}_i = \frac{1}{2}\sum_{\sigma,\sigma'} \hat{c}^{\dagger}_{i\sigma}\vec{\sigma}_{\sigma\sigma'}\hat{c}_{i\sigma'}$, where $\vec{\sigma}$ is the vector of Pauli matrices. During all the calculations that follow, we have assumed a hyperfine interaction with values[29] $\Delta_i^{(z)} = [0.15, 0.2, 0.1, 0.14]\,\mu$eV. The main conclusions of the paper are independent of the specific values of the hyperfine interaction, as long as they are in the range of typical values for GaAs QDs.

We restrict our analysis to the lowest orbital state in each QD, assuming that the orbital level spacing is much larger than both the thermal energy and the tunneling amplitudes, such that excited orbitals remain effectively unpopulated. Although higher orbitals could, in principle, open additional transport channels or renormalize the effective interactions, such effects are strongly suppressed in the experimentally relevant regime considered here. Our model is formulated for GaAs, where valley degrees of freedom are absent. However, the core mechanism, namely, long-range transfer mediated by virtual transitions, is expected to remain applicable to silicon QDs as well, provided the valley splitting exceeds both the tunneling amplitudes and thermal energy, $\Delta_{\text{VS}} \sim 250\,\mu\text{eV} \gg \tau_i \sim 10\,\mu\text{eV}$, $k_BT \sim 1\,\mu$eV[46–48]. Nevertheless, valley splitting must be taken into account in regimes where high detuning brings excited orbital states into resonance. Such scenarios lie outside the scope of this work. Finally, in systems with small or fluctuating valley splitting, transport resonances may broaden or split, complicating the identification of coherent long-range transfer.

For simplification, we assume that the inter-dot Coulomb repulsion depends only on the distance between the dots, i.e., $V_k \equiv V_{i,i+k}$. The on-site energies are determined by the applied voltage bias. Due to capacitive cross-talk, these energies are not independent, and are expressed as a linear combination of the voltages applied to the two outermost gates, see Fig. 1b, as

$$\varepsilon_i = \varepsilon_{i0} + \alpha_{iL}V_L + \alpha_{iR}V_R, \tag{2}$$

where ε_{i0} is a static energy offset, $\alpha_{iL(R)}$ is the lever arm associated with the left (right) gate, and $V_{L(R)}$ is the corresponding voltage bias. Without loss of generality, we set the energy offsets of the first and last dots to zero, i.e., $\varepsilon_{10} = \varepsilon_{N0} = 0$. For concreteness, we adopt the lever arm values[37]: $\alpha_{iL} = (-85, -36, -12, -7)\,\mu\text{eV mV}^{-1}$ and $\alpha_{iR} = (-7, -12, -32, -81)\,\mu\text{eV mV}^{-1}$.

Model for open system

The leads are modeled by the Hamiltonian

$$\hat{H}_{\text{leads}} = \sum_{l=L,R}\sum_{k}\sum_{\sigma} \varepsilon_{lk}\hat{d}^{\dagger}_{lk\sigma}\hat{d}_{lk\sigma}, \tag{3}$$

where $\hat{d}^{\dagger}_{lk\sigma}$ ($\hat{d}_{lk\sigma}$) creates (annihilates) an electron in lead l with momentum k, spin σ, and energy ε_{lk}.

Finally, the coupling between the leads and the QDs is described by

$$\hat{H}_{\text{coup}} = \sum_{l,k,i,\sigma}\left(\gamma_{l,i}\hat{d}^{\dagger}_{lk\sigma}\hat{c}_{i\sigma} + \text{H.c.}\right), \tag{4}$$

where $\gamma_{l,i}$ quantifies the coupling strength between lead l and dot i. We assume a linear array of N dots, with the first and last dots coupled to the left and right leads, respectively. Thus, the nonzero couplings are $\gamma_{L,1} = \gamma_L$ and $\gamma_{R,N} = \gamma_R$, while $\gamma_{L,i} = \gamma_{R,i} = 0$ for all other sites.

The charge current is obtained by solving the steady-state of the Lindblad master equation for the reduced density matrix of the dots[49]:

$$\dot{\hat{\rho}}_{\text{ss}} = -i[\hat{H}_0, \hat{\rho}_{\text{ss}}] + \mathcal{L}\hat{\rho}_{\text{ss}} = 0. \tag{5}$$

Here, $\hat{\rho}_{\text{ss}}$ is the steady state reduced density matrix of the dots, and the Liouvillian superoperator $\mathcal{L}$ accounts for the coupling to the leads, as well as spin relaxation and dephasing processes. A detailed derivation of the Lindblad master equation is provided in the Supplementary Methods. For all the simulations presented in this work, unless otherwise stated, we consider the coupling to the leads as $\Gamma_L = 0.28\,\mu$eV and $\Gamma_R = 0.21\,\mu$eV, where $\Gamma_{L(R)} = 2\pi\mathcal{D}_{L(R)}|\gamma_{L(R)}|^2$, and $\mathcal{D}_{L(R)}$ is the density of states of the leads.

In our model, the main decoherence mechanisms included are spin relaxation (T_1) and spin dephasing (T_2), which enter the Lindblad equation as incoherent processes. We do not include explicit mechanisms for charge relaxation or pure charge dephasing. However, we study the primary impact of charge dephasing on the charge transport properties in the Supplementary Note 1.

Our primary objective is to analyze long-range transport across a QQD array, with electric current flowing from the left to right. To this end, we examine the charge current as a function of the gate voltages applied to the extremes of the quantum dot array. To compute the current operator, we assume a positive bias direction, i.e., $\mu_L > \mu_R$, where μ_l is the chemical potential of lead l. Therefore, the charge current for the QQD is given by

$$I_{\text{QQD}} = esum_{m,n}\left(\Gamma^{+}_{mn}\rho^{\text{ss}}_{nn} - \Gamma^{-}_{mn}\rho^{\text{ss}}_{nn}\right), \tag{6}$$

where Γ^{+}_{mn} is the transition rate from state $|m\rangle$ to state $|n\rangle$ due to a tunneling event from the quantum dot array to one lead, and analogous for Γ^{-}_{mn} for a

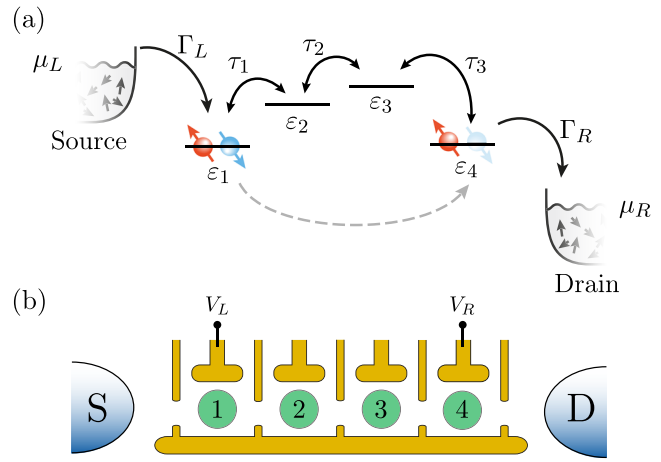

Fig. 1 | Schematic figure of the total system. a Linear quadruple quantum dot (QQD) array, coupled to leads with rates $\Gamma_{L,R}$, defined by chemical potentials $\mu_{L,R}$. Electrons can flow from the source (left lead) to the drain (right lead) through the quantum dot array. Interdot tunneling rates are denoted by τ_i. Each dot is characterized by its on-site energy ε_i. When states (2, 0, 0, 1) and (1, 0, 0, 2) are degenerate, and the middle dots are out of resonance, long-range transport occurs between the first and last dots, denoted with a gray dashed line. **b** Gates defining the QQD, together with the source and drain leads. The plunger states V_L and V_R are applied to the first and fourth dots, respectively.

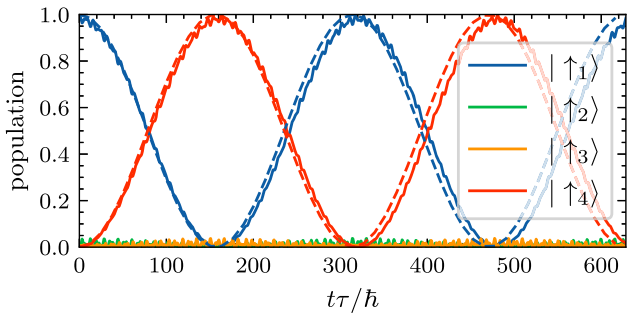

Fig. 2 | Dynamics of the charge occupation for a single particle in a closed quadruple quantum dot. The dynamics is represented for the original Hamiltonian (solid lines), and the effective model (dashed lines), given by Eq. (8). The system parameters are $\tau_i = \tau$, $\varepsilon_1 = \varepsilon_4 = 0$, and $\varepsilon_2 = \varepsilon_3 = 10\tau$.

tunneling event from one lead to the quantum dot array. Here, ρ^{ss}_{nn} is the diagonal element of the density matrix in the steady state, which is obtained by solving Eq. (5) with $\dot{\rho}_{mn} = 0$.

We now introduce the notation for the quantum states considered. Focusing on the charge sector, basis states are labeled by the site occupations as $|n_1, n_2, n_3, n_4\rangle$. The corresponding energy is denoted E_{n_1,n_2,n_3,n_4}. In absence of an external magnetic field, these energies are independent of spin. However, due to the presence of Coulomb interaction, the eigenenergies lift the degeneracy between states with different spin configurations.

Throughout this manuscript, we consider configurations with a total electron number ranging from 0 to 4. Simulations involving larger occupation numbers (from 5 to 8 electrons) yield qualitatively similar results.

In this manuscript, we focus specifically on long-range transitions between the first and last dots in the QQD array. To facilitate this, we define a dark state $|DS\rangle$ as an eigenstate of the system Hamiltonian that exhibits zero population on the two central dots. It is important to note that this definition of a dark state originates within the quantum state transfer framework[50–52] and differs from its usage in the context of charge transport, where a dark state is typically understood as one that does not contribute to current flow[12,31].

Results and discussion

One particle results

Closed system. We begin by analyzing the dynamics of a single electron in an isolated QQD array, i.e., with $\Gamma_{L,R} = 0$. In this regime, the spin degree of freedom can be neglected, and the Hamiltonian simplifies to

$$\hat{H}_0 = \sum_{i=1}^{N=4} \varepsilon_i \hat{n}_i + \sum_{i=1}^{N-1=3} \tau_i \left(\hat{c}_i^\dagger \hat{c}_{i+1} + \text{H.c.} \right), \tag{7}$$

where we have neglected the hyperfine interaction term.

An exact diagonalization reveals that, in contrast to the TQD case, a dark state is not present in the QQD array, even when all dots are in resonance $\varepsilon_i = \varepsilon$. That is, there exists no eigenstate of the Hamiltonian exhibiting an exact vanishing occupation of the central dots, see the Supplementary Note 2 for more details.

Nonetheless, a high-order co-tunneling process can emerge when the central dots are strongly detuned from the outer ones, enabling direct tunneling between the first and last dots. The occupation of the intermediate dots can be suppressed by tuning their on-site energies ε_i. In the limit $|\varepsilon_2|, |\varepsilon_3| \gg |\varepsilon_1|, |\varepsilon_4|, \tau_i$, a third-order Schrieffer-Wolff transformation yields an effective Hamiltonian involving only the outermost dots:

$$\hat{H}_{\text{eff}} = \tilde{\varepsilon}_1 \hat{n}_1 + \tilde{\varepsilon}_4 \hat{n}_4 + \tau_{\text{eff}} \left(\hat{c}_1^\dagger \hat{c}_4 + \text{H.c.} \right), \tag{8}$$

where the renormalized on-site energies are $\tilde{\varepsilon}_1 = \varepsilon_1 + \tau_1^2/(\varepsilon_1 - \varepsilon_2)$ and $\tilde{\varepsilon}_4 = \varepsilon_4 + \tau_3^2/(\varepsilon_4 - \varepsilon_3)$, and the effective hopping amplitude is

$$\tau_{\text{eff}} = \frac{\tau_1 \tau_2 \tau_3}{2} \left[\frac{1}{(\varepsilon_1 - \varepsilon_2)(\varepsilon_1 - \varepsilon_3)} + \frac{1}{(\varepsilon_4 - \varepsilon_2)(\varepsilon_4 - \varepsilon_3)} \right]. \tag{9}$$

In the Supplementary Note 3, we provide a brief introduction to the Schrieffer-Wolff transformation and the derivation of the above effective Hamiltonian.

When the condition $\tilde{\varepsilon}_1 = \tilde{\varepsilon}_4$ is met, full charge transfer between the outermost dots becomes possible with negligible population of the central sites. This transfer is mediated by virtual transitions to the central dots, which are energetically forbidden. Figure 2 illustrates how the dynamics governed by the effective model closely replicate those of the full Hamiltonian, with Rabi oscillations between the first and last dots (blue and red lines), and minimal occupation of the intermediate dots (green and orange lines). The rapid wiggling of the solid lines indicates the presence of coherent oscillations, which are not present in the effective model (dashed lines). These low amplitude oscillations are a consequence of the small but finite population of the central dots, with a maximum population of ~3% on each of them. Increasing the detuning of the central dots $|\varepsilon_2|, |\varepsilon_3|$ leads to a suppression of these oscillations, at the expense of reducing the effective tunneling amplitude τ_{eff}, which in turn reduces the Rabi oscillation frequency. Working with a moderate tunneling rate of $\tau_i \sim 1\,\mu$eV, we estimate a transfer time ~100 ns. This timescale is lower than the typical charge fluctuation time in GaAs QDs, which is on the order of 1 ms[53,54], indicating that the long-range transfer can be achieved within the coherence time of the system.

Open system. When the QQD is coupled to the electronic reservoirs, a current can flow through the system. This occurs only when a resonant transition within the QQD is energetically allowed, and it is inside the transport window. For a single particle, the region of positive charge current is defined by the conditions $\mu_L \geq \varepsilon_1$ and $\mu_R \leq \varepsilon_4$. Outside this region, the system resides in a Coulomb blockade regime, and the current vanishes.

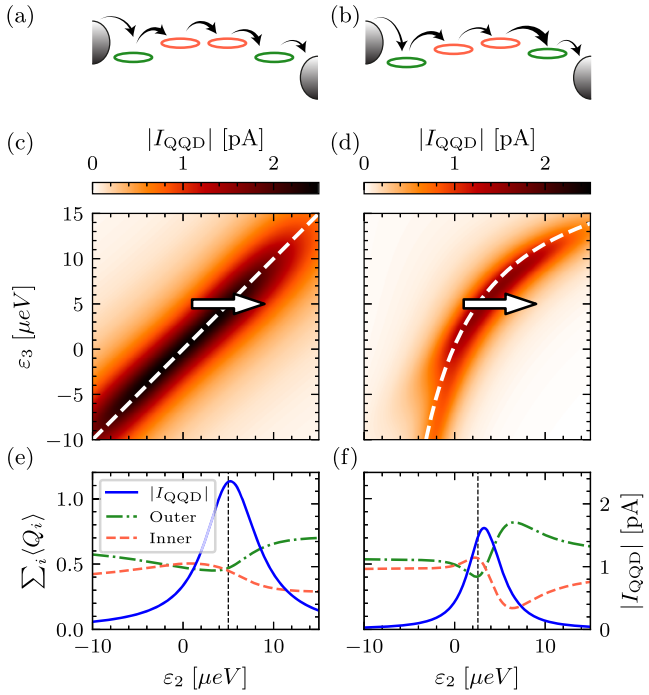

Fig. 3 | Current and average charge in a quadruple quantum dot with a single particle. Schematic representation of the system in a (**a**) highly symmetric configuration, and (**b**) an asymmetric configuration. The green ellipses denote the outer dots, while the red ellipses denote the inner dots. The half circles represent the leads, and the arrows indicate the tunneling directions with its thickness representing the tunneling rates. **c**, **d** show the current on the quadruple quantum dot (I_{QQD}) as a function of the detunings ε_2 and ε_3. White dashed lines denote the analytical resonance condition from Eq. (10). **e**, **f** show the average charge (left axis) and current (right axis) along the white horizontal arrows in panels (**c**, **d**), with $\varepsilon_3 = 5$ μeV. Green dot-dashed lines represent average charge in the outer dots, red dashed lines for the inner dots, and the blue solid lines indicate the current. Vertical dashed lines mark the position of the resonance. The parameters for the symmetric case (**c**, **e**) are $\tau_i = [2, 2, 2]\,\mu$eV and $\varepsilon_1 = \varepsilon_4 = 0$, while for the asymmetric case (**d**, **f**) are $\tau_i = [2, 1, 3]\,\mu$eV, $\varepsilon_1 = 0$, and $\varepsilon_4 = 0.4$ μeV.

Using the effective model from Eq. (8), the resonance condition $\tilde{\varepsilon}_1 = \tilde{\varepsilon}_4$ results in the relation

$$\varepsilon_3 = \varepsilon_4 + \frac{\tau_3^2(\varepsilon_2 - \varepsilon_1)}{\tau_1^2 + (\varepsilon_1 - \varepsilon_2)(\varepsilon_1 - \varepsilon_4)}. \tag{10}$$

It is important to remark that when the condition of large detuning between the outer and the inner dots is not fulfilled, the effective model is no longer valid. In this case, even with $\tilde{\varepsilon}_1 = \tilde{\varepsilon}_4$, the population of the middle dots remains finite. To quantify the average charge occupation of each dot, we define

$$\langle Q_i \rangle \equiv \mathrm{tr}(\hat{n}_i \hat{\rho}_{ss}). \tag{11}$$

Figure 3 presents the charge current for the QQD, as a function of detunings ε_2 and ε_3 for two distinct configurations. We observe typical currents in the range of $I_{QQD} \sim 2$ pA, which are measurable in state-of-the-art experiments[29]. Based on this current, we estimate that the average time to transfer a single electron across the QQD is in the order of $t_{QQD} = e/I_{QQD} \sim 100$ ns, which coincide with the timescale of the Rabi oscillations in the effective model. Note that this time is larger than the spin dephasing time $T_2 = 10$ ns, indicating that the main features of the long-range transport are not significantly affected by the spin dephasing. We will study this effect in more detail in the Multiple particle results subsection in the Results and Discussion section.

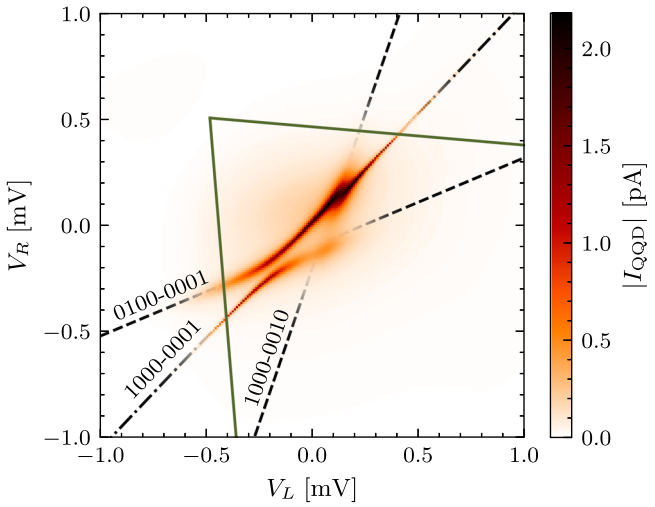

Fig. 4 | Current through the quadruple quantum dot array in the single-particle regime. The current is shown as a function of the gate voltages applied to the left- and right-most dots, V_L and V_R, respectively. Dark green lines denote the region of positive charge current, as described in Eq. (13). Black lines indicate various resonance conditions. Dashed lines correspond to long-range transfers between first and third, and second and fourth dots. With a dot-dashed line we denote a long-range transition between the first and last dots. Lines fade out in regions of high current to emphasize the current features. The parameters are $\tau_i = [3, 5, 2]\,\mu$eV, $T_2 = 10$ ns, $\mu_{L(R)} = \pm 37.5$ μeV, $\varepsilon_{20} = 7$ μeV, and $\varepsilon_{30} = -5$ μeV.

In the symmetric case, Fig. 3c–e, tunneling amplitudes are equal for all dots, and the outer dots are in resonance. A pronounced current resonance appears, though the population of the central dots remains non-zero, i.e., $\langle Q_2 \rangle + \langle Q_3 \rangle \neq 0$. In the case of larger detuning for the inner dots, its population is reduced. However, the effective tunneling amplitude τ_{eff} drastically decreases, leading to a reduced current that is hard to observe in real experiments.

To compare results, we also study an asymmetric configuration in Fig. 3d–f, not only in terms of the on-site energies of the outer dots, but also in the tunneling rates. In contrast to the symmetric configuration, close to the resonant condition, a clear dip in the central dots population emerges. In this situation, the central dots hybridize effectively, forming a single dot. The resulting dynamics resemble those of a TQD, which supports a dark state with vanishing central dot population.

Importantly, even in TQD systems coupled to the leads, where dynamics become incoherent, the central dot population is no longer strictly zero, but still exhibits a pronounced dip close to the resonance, similar to the one shown in Fig. 3f. Such a dip is absent in the symmetric QQD configuration. This observation underscores that long-range transport does not necessarily require a highly symmetric configuration. Furthermore, the presence of a finite dephasing time T_2 modifies both the current and the inner dots' occupation, as can be seen in the Supplementary Note 1. As expected, systems with low dephasing times exhibit a less pronounced dip in the inner dots' occupation, making it difficult to observe long-range transport.

So far, we have focused on tuning the on-site energies to gain intuitive insight into the system's behavior. However, capacitive coupling among the dots significantly alters the resonance conditions. Nevertheless, based on prior results, we expect that transport signatures persist even under asymmetries induced by lever arms. In Fig. 4, we show the charge current as a function of the gate voltages V_L and V_R.

In general, the transport window for the resonance between two states $|\psi_1\rangle = |n_1, n_2, \ldots, n_N\rangle$ and $|\psi_2\rangle = |n_1', n_2', \ldots, n_N'\rangle$, with associated energies E_{ψ_1} and E_{ψ_2}, is defined by the conditions

$$\begin{aligned} \mu_L &\geq E_{\psi_1} - E_{\psi_1^{(L)}}, \\ \mu_R &\leq E_{\psi_2} - E_{\psi_2^{(R)}}, \end{aligned} \tag{12}$$

Table 1 | Spin basis of single occupied states for three electrons

Basis	s	s_z	Tensor basis
$\|Q_{ijk}^{(+3/2)}\rangle$	3/2	+ 3/2	$\|\uparrow_i\uparrow_j\uparrow_k\rangle$
$\|Q_{ijk}^{(+1/2)}\rangle$	3/2	+ 1/2	$\frac{1}{\sqrt{3}}\left(\|\downarrow_i\uparrow_j\uparrow_k\rangle+\|\uparrow_i\downarrow_j\uparrow_k\rangle+\|\uparrow_i\uparrow_j\downarrow_k\rangle\right)$
$\|Q_{ijk}^{(-1/2)}\rangle$	3/2	− 1/2	$\frac{1}{\sqrt{3}}\left(\|\downarrow_i\downarrow_j\uparrow_k\rangle+\|\uparrow_i\downarrow_j\downarrow_k\rangle+\|\downarrow_i\uparrow_j\downarrow_k\rangle\right)$
$\|Q_{ijk}^{(-3/2)}\rangle$	3/2	− 3/2	$\|\downarrow_i\downarrow_j\downarrow_k\rangle$
$\|D_{ijk}^{(+1/2)}\rangle$	1/2	+ 1/2	$\frac{1}{\sqrt{2}}\left(\|\uparrow_i\downarrow_j\uparrow_k\rangle-\|\downarrow_i\uparrow_j\uparrow_k\rangle\right)$
$\|D_{ijk}^{(-1/2)}\rangle$	1/2	− 1/2	$\frac{1}{\sqrt{2}}\left(\|\uparrow_i\downarrow_j\downarrow_k\rangle-\|\downarrow_i\uparrow_j\downarrow_k\rangle\right)$
$\|D_{ijk}^{\prime(+1/2)}\rangle$	1/2	+ 1/2	$\frac{1}{\sqrt{6}}\left(2\|\uparrow_i\uparrow_j\downarrow_k\rangle-\|\uparrow_i\downarrow_j\uparrow_k\rangle-\|\downarrow_i\uparrow_j\uparrow_k\rangle\right)$
$\|D_{ijk}^{\prime(-1/2)}\rangle$	1/2	− 1/2	$-\frac{1}{\sqrt{6}}\left(2\|\downarrow_i\downarrow_j\uparrow_k\rangle-\|\downarrow_i\uparrow_j\downarrow_k\rangle-\|\uparrow_i\downarrow_j\downarrow_k\rangle\right)$

The indices $1\le i\ne j\ne k\le N$ denote the QDs where the electrons are located.

where we have defined the states $|\psi^{(L)}\rangle=|n_1-1,n_2,\ldots,n_N\rangle$ and $|\psi^{(R)}\rangle=|n_1,n_2,\ldots,n_N-1\rangle$ as the states with one fewer electron in the left- and right-most dots, respectively, and their corresponding energies $E_{\psi^{(L)}}$ and $E_{\psi^{(R)}}$. Across the entire work, we will denote the region of positive current with dark green lines for the long-range transfer between the first and last dots. In this subsection, we show the transport window for the states $|\psi_1\rangle=|1000\rangle$ and $|\psi_2\rangle=|0001\rangle$, obtaining:

$$\begin{aligned}\mu_L\ge\varepsilon_1 &= \alpha_{1L}V_L+\alpha_{1R}V_R,\\ \mu_R\le\varepsilon_4 &= \alpha_{4L}V_L+\alpha_{4R}V_R.\end{aligned}\tag{13}$$

The transport window for other states can be obtained by using the condition in Eq. (12) with the corresponding energies. Out of the transport window, a small but finite current flows due to the finite temperature. Inside the transport triangle, the current is maximum in a series of resonance conditions, which are represented by the black lines. These resonances are due to the possibility of a resonant transition between different energy levels of the QQD. On the one hand, we have the long-range transfer between the first and last dot of the array, labeled as 1000–0001. Note that we have dropped kets in the states in order to simplify the notation. On the other hand, other long-range transitions between the next nearest-neighbor dots, labeled as 0100–0001, and 1000–0010, are also present. When these transitions meet, the current exhibits an avoiding crossing, which is a clear signature of different coherent processes interfering with each other.

Black lines in Fig. 4 represent solutions to the resonance conditions. As an example, for the 1000–0001 resonance we solve $\varepsilon_1=\varepsilon_4$, obtaining the condition

$$V_R=V_L\frac{\alpha_{4L}-\alpha_{1L}}{\alpha_{1R}-\alpha_{4R}}.\tag{14}$$

By fitting the slope of this resonance, the corresponding lever arms can be extracted.

We conclude that, even in the presence of decoherence and reduced symmetry, manifested through detuned central dots and non-uniform tunneling rates, the 1000–0001 long-range resonance remains observable. In the Supplementary Note 1, we include a study of the effect of charge dephasing on the current, showing that, even when working with state-of-the-art dephasing times, long-range transport is still visible.

Multiple particle results

Closed system. The dynamics of the QQD array become significantly richer when multiple electrons are introduced into the system. Here, we concentrate on the scenarios involving two and three electrons.

Since the original Hamiltonian described in Eq. (1) in absence of hyperfine interaction preservers total spin, the Hilbert space decomposes naturally into subspaces labeled by the total spin quantum number s. For two electrons, the total spin can adopt values of $s=1$ (triplet states, T) or $s=0$ (singlet states, S). In the case of three electrons, the total spin can adopt values of $s=3/2$ (quartet states, Q) or $s=1/2$ (doublet states, D). We employ Clebsch-Gordan coefficients to represent these spin states, given in Table 1. In addition to these single-occupied states, doubly occupied states, denoted by $|S_i\sigma_j\rangle$, indicating a double occupancy at site i and single occupancy with spin σ at site $i\ne j$, also become relevant.

In practice, slow variations in the local Zeeman splitting, arising from nuclear spin dynamics or g-factor inhomogeneity, break total spin conservation on microsecond timescales. However, since the considered local Zeeman splitting is smaller than the coupling rates $\Delta_i^{(z)}\ll\tau_i$ and the transport dynamics of interest occur on the order of ~ 100 ns, spin remains a good quantum number over the relevant interval.

The system's dynamics are thus enriched by competing coherent processes. To elucidate the underlying physics, it is instructive to analyze each spin sector independently. The simplest scenario is the $s=3/2$ subspace, where double occupancies are forbidden. It is worth noting that no spin-flip processes are present in the closed system, so no coupling between quartets and double-occupied states is possible. Under these conditions, the sector closely resembles the single-particle, admitting long-range transfer when $E_{1110}=E_{0111}$. In such conditions, the central dots are maximally occupied, yet exhibit no charge fluctuations during dynamics. This resonance condition coincides exactly with the single-particle resonance given by Eq. (14). Using Eq. (12), we find that the condition for positive current in this regime is $\mu_L\ge(E_{1110}-E_{0110})$ and $\mu_R\le(E_{0111}-E_{0110})$. Near resonance, we derive an effective two-state Hamiltonian effective model given by:

$$\begin{aligned}\hat{H}_{\text{eff}}=&\tilde{E}_{1110}\left|Q_{123}^{(+3/2)}\right\rangle\left\langle Q_{123}^{(+3/2)}\right|\\&+\tilde{E}_{0111}\left|Q_{234}^{(+3/2)}\right\rangle\left\langle Q_{234}^{(+3/2)}\right|\\&+\tilde{\tau}\left(\left|Q_{123}^{(+3/2)}\right\rangle\left\langle Q_{234}^{(+3/2)}\right|+\text{H.c.}\right),\end{aligned}\tag{15}$$

where the effective energies and hopping amplitudes can be found in the Supplementary Note 4. By making the substitutions $E_{1110}\to\varepsilon_4$, $E_{1101}\to\varepsilon_3$, $E_{1011}\to\varepsilon_2$, and $E_{0111}\to\varepsilon_1$, we directly mapped to a single-particle scenario by reinterpreting the process as hole transport between the outermost dots. In the equation above we have focused on the $s_z=+3/2$ sector, but the same results can be obtained for all the other s_z values.

In the $s=1/2$ subspace, analogous long-range transfer conditions ($E_{1110}=E_{0111}$) remain valid. However, due to degeneracy between doublet states $|D_{ijk}^{(\sigma)}\rangle$ and $|D_{ijk}^{\prime(\sigma)}\rangle$ in the absence of magnetic fields, the resulting effective model is significantly more intricate, making the mapping to a single-particle systems less straightforward.

Alternatively, double occupancy states permit another type of long-range transport under the resonance $E_{2001}=E_{1002}$, characterized by minimal intermediate-dot occupancy. An effective Hamiltonian describing this case reads

$$\begin{aligned}\hat{H}_{\text{eff}}=&\tilde{E}_{2001}|S_1\downarrow_4\rangle\langle S_1\downarrow_4|+\tilde{E}_{1002}|S_4\downarrow_1\rangle\langle S_4\downarrow_1|\\&+\tilde{\tau}\left(|S_1\downarrow_4\rangle\langle S_4\downarrow_1|+\text{H.c.}\right),\end{aligned}\tag{16}$$

where the effective energies and hopping amplitudes can be found in the Supplementary Note 5. Figure 5 shows the dynamics of the closed system, which demonstrates that this effective model accurately captures the system's dynamics. At the bottom, we present a zoomed-in view of the dynamics for the central dots, showing a population lower than 1%. Due to this small population, the rapid oscillations for the outer dots, presented in Fig. 2, are highly suppressed.

Here, we have shown the dynamics for the case of three particles, but similar results can be obtained for two particles for the long-range resonances 2000–1001 and 1100–0101.

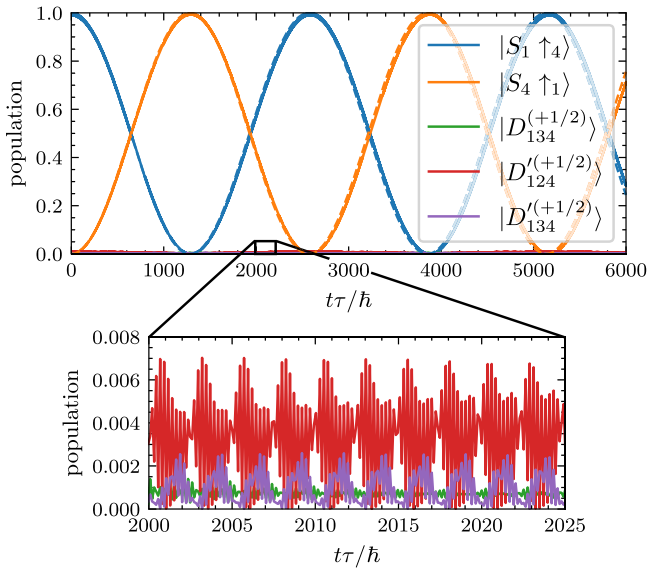

Fig. 5 | Dynamics of the charge occupation for three particles in a closed quadruple quantum dot. The dynamics is shown for the original Hamiltonian (solid lines), and the effective model (dashed lines), from Eq. (16). In the bottom, a zoomed-in view of the dynamics is shown, to better visualize the small population of the central dots. System parameters are given by $\tau_i = \tau = 3\,\mu$eV, $\varepsilon_i = [-1836.2, -700, -655, -1714]\,\mu$eV, $U_i = [1720, 1500, 1220, 1600]\,\mu$eV, $V_i = [450, 200, 100]\,\mu$eV.

Open system. Coupling the QQD to leads enables a finite current to flow under suitable resonance conditions. A general resonance between two charge configurations, $|n_1, n_2, n_3, n_4\rangle$ and $|n'_1, n'_2, n'_3, n'_4\rangle$, is described by a straight line in the V_L-V_R plane. Solving the resonance condition $E_{n_1,n_2,n_3,n_4} = E_{n'_1,n'_2,n'_3,n'_4}$, the resulting line takes the form $V_R = mV_L + n$, where the slope is given by

$$m = \frac{\sum_{i=1}^{4} \alpha_{iL}(n_i - n'_i)}{\sum_{i=1}^{4} \alpha_{iR}(n'_i - n_i)}. \tag{17}$$

Note that, in general, the slope m is not unique, and different resonances may exhibit the same slope. For example, the transitions 2000–1001 and 1100 − 0101 share the same value of m. The intercept n is determined by the Coulomb interaction and the on-site energies ε_{20} and ε_{30}, defined in Eq. (2). It is this intercept that breaks the slope degeneracy, allowing us to distinguish between different resonance lines. However, since the explicit expression for n is lengthy and not relevant for the current discussion, its derivation is provided in the Supplementary Note 6.

In Fig. 6a, we show the charge current near the 1100–0101 transition. In this case, both singlet and triplet states contribute to the transport. Since we are dealing with multiple resonance conditions with different initial and final states, the transport triangle differs for each resonance condition. This difference is clearly visible in the 1100–1001 resonance, where the current rapidly decreases for $V_L > -1$ mV. At the intersection of the 1100–0110 and 1100–0101 resonances, we observe a pronounced current drop.

This current blockade is a consequence of the resonance between the first and third dots. To gain better insight into the current blockade, we focus on the 1100–1001 resonance. For this resonance, out of the blockade region, the current follows the path 1000 → 0100 → 1100 → 1001 → 1000. The first step is the bottleneck of the process, since other paths are in resonance. That is why, if the first and the second dots are in resonance, the current is maximized, see Fig. 6b, c. However, when the first and the third dots are in resonance, the path is given by 1000 → 0010 → 1010. The final state is out of the transport window, and the current is blockaded, leading a sharp drop in the current. Since double occupancy states are not involved in the blockade, the same mechanism explains the blockade of triplet and singlet states. If the

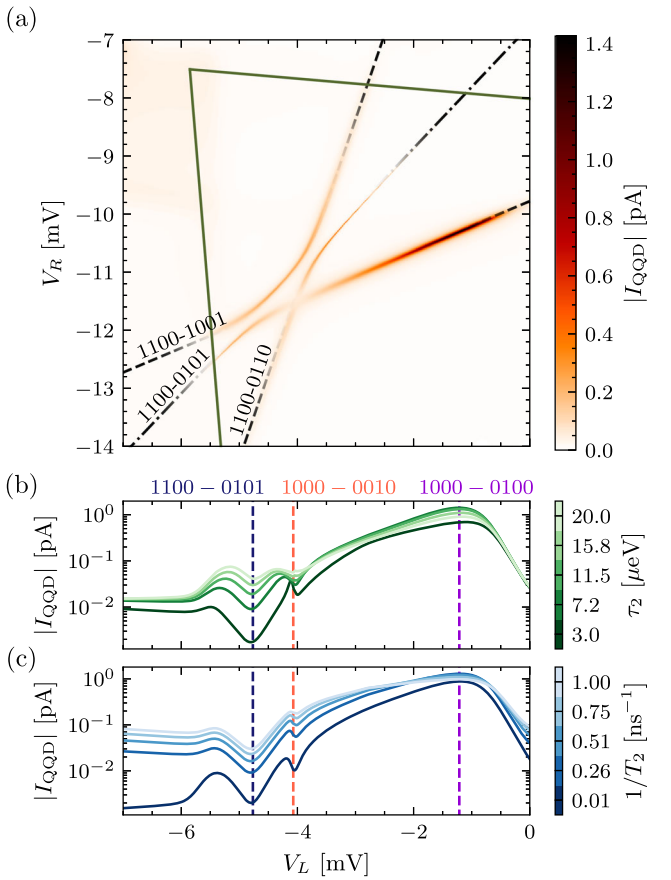

Fig. 6 | Current in the two-particle regime near the 1100 − 0101 resonance. **a** Current map as a function of the gate voltages applied to the left- and right-most dots, V_L and V_R, respectively. Dark green lines indicate the region of positive current. Black dashed and dot-dashed lines correspond to different resonance conditions, as labeled. **b**, **c** Current blockade for the 1100–1001 resonance. In (**b**), we show the current for different values of the central tunneling amplitude τ_2 for $T_2 = 10$ ns, and in (**c**), we show the current for different values of the dephasing time T_2 with $\tau_2 = 5$ μeV. Vertical color-coded dashed lines indicate the position for the resonances denoted on (**a**). Other parameters, common to all panels, are $\varepsilon_{20} = 8$ μeV and $\varepsilon_{30} = 10$ μeV, $U_i = [1500, 1650, 1220, 1800]\,\mu$eV, $V_i = [1000, 500, 333]\,\mu$eV, $\tau_i = [10, 20, 10]\,\mu$eV, and $\mu_L = 1550$ μeV and $\mu_R = 1250$ μeV. All other parameters are identical to those in Fig. 4.

tunneling rate between the second and the third dots is increased, even if there are out of resonance, a finite current can flow through the system, obtaining a less pronounced blockade, as shown in Fig. 6b. When the dephasing time is reduced, see Fig. 6c, the current blockade is slightly lifted, but a clear current drop is still present.

It is important to note that the blockade also coincides with the resonance $E_{1100} = E_{1001} = E_{0110}$. However, the presence of the state $|0110\rangle$ is not necessary for the blockade to occur. This coincidence is due to the fact that the interdot Coulomb repulsion is site independent, i.e, the repulsion energy between two particles located between the first and the second dots is the same as between the second and the third dots. The result is that the resonant condition for the 1100–0110 transition is given by the same condition as the 1000–0010 transition.

By modifying the bias voltage, and the detuning of the central dots, we can focus on resonance conditions such that singlet states are mainly involved in the transport while reducing the presence of triplet states, as shown in Fig. 7. Here, only the resonance condition 1100–1001 carry any contribution from the triplet states, as demonstrated by the absence of an avoided crossing between the 2000–1001 and 1100–0101 transitions. In the upper right corner, marked with a white arrow, we observe a fine line with high current which corresponds to a three-particle resonance, given by

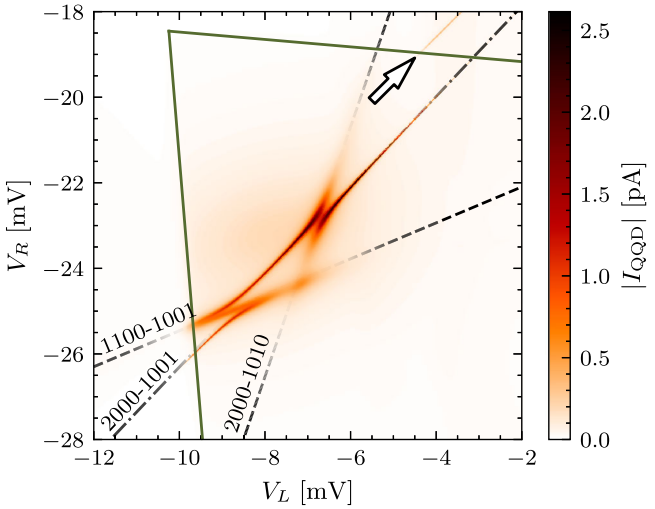

Fig. 7 | Current map in the two-particle regime near the 2000 − 1001 resonance. The current is shown as a function of the gate voltages applied to the left- and right-most dots, V_L and V_R, respectively. Dark green lines indicate the region of positive current. Black dashed and dot-dashed lines correspond to different resonance conditions, as labeled. The detuning of the central dots is $\varepsilon_{20} = 800$ μeV and $\varepsilon_{30} = 9203.7$ μeV, and the bias are $\mu_L = 2500$ μeV and $\mu_R = 1900$ μeV. A white arrow indicates the 2010–1101 resonance. All other parameters are identical to those in Fig. 6.

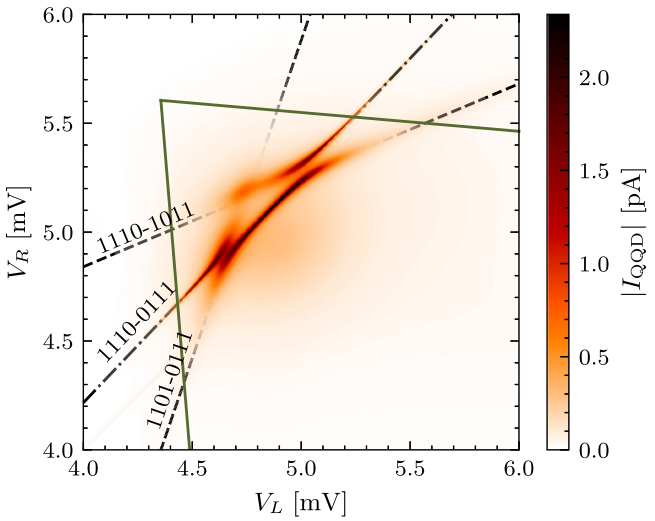

Fig. 8 | Current map in the three-particle regime near the 1110–0111 resonance. The current is shown as a function of the gate voltages applied to the left- and right-most dots, V_L and V_R, respectively. Dark green lines indicate the region of positive current. Black dashed and dot-dashed lines correspond to different resonance conditions, as labeled. The detuning of the central dots is $\varepsilon_{20} = \varepsilon_{30} = -398$ μeV, and the Coulomb repulsion is $U_i = [1720, 1500, 1220, 1600]\,\mu$eV, $V_i = [280, 167, 100]\,\mu$eV. All other parameters are identical to those in Fig. 4.

2010–1101. This resonance is interesting since it corresponds to a tunneling involving two electrons, in contrast to the previous cases, where only one electron was involved in the tunneling process.

Going beyond the two-particle regime, more interesting phenomena can be found when including an extra particle as show in Fig. 8, where we show the charge current near the 1110–0111 transition. Here, both quartet and doublet states contribute to the transport. Although there are no doubly occupied states involved, long-range transfer remains possible. The results bear a resemblance to the single-particle case, as seen by comparing with Fig. 4 after applying the transformation $V_{L(R)} \to -V_{R(L)}$. This symmetry arises from the interpretation of the 1110–0111 resonance as a long-range hole transfer, equivalent to a single positively charged particle moving from right to left.

The resonance condition for the 2001–1002 transition is given by

$$V_R = \frac{V_L(\alpha_{4L} - \alpha_{1L}) + U_4 - U_1}{\alpha_{1R} - \alpha_{4R}}, \tag{18}$$

while the condition for positive current is $\mu_L > (E_{2001} - E_{1001})$ and $\mu_R < (E_{1002} - E_{1001})$. However, one must ensure that this transport window does not overlap with the regions where a fourth electron can enter the system, which would significantly suppress the current. To avoid this, we impose the additional constraints $\mu_L < (E_{1111} - E_{0111})$ and $\mu_R > (E_{1110} - E_{1111})$. Although the resonance condition is independent of $\mu_{L(R)}$, the positive current region depends explicitly on the chemical potentials of the leads. These can be parametrized as $\mu_{L(R)} = \mu_0 \pm \Delta\mu/2$. With this formulation, μ_0 shifts the transport triangle across the $V_L = V_R$ line, while $\Delta\mu$ displaces it along the $V_L = -V_R$ direction.

To satisfy the above constraints while avoiding the addition of an extra particle, the system parameters must be selected carefully, with particular attention to the interdot Coulomb interactions V_i. We find that, for fixed values of all other parameters, there exists only a narrow window of V_i where a positive current and visible long-range transfer coexist. This regime typically occurs for large values of V_i.

Figure 9a displays the charge current as a function of the gate voltages V_L and V_R for a representative set of parameters. The chosen configuration is one of many that yields a high-current region associated with long-range transfer. The resulting current is highly similar to the two-particle case shown in Fig. 7. This similarity arises since the particle stuck in the last dot does not affect the dynamics of the system, and only renormalizes the different energies. Then, this particle can be traced out, leading to an effective model with only two particles. Due to the complexity of the system, multiple parameter combinations can produce similar results. Here, we observe three distinct long-range transitions, 2001–1002, 1110–1002, and 2001–1011, each indicated by black lines. At the intersections of these transitions, the current exhibits avoided crossings, which signal interference between coherent transport processes. This is particularly clear in the upper right region, where the 2001–1002 and 2001–1011 cross.

In contrast, at the crossing between 2001–1002 and 1101–1002, shown in the zoomed view in Fig. 9a, a straight unperturbed resonance line appears. To understand this behavior, we analyze the effective model near the triple degeneracy point $E_{2001} = E_{1002} = E_{1101}$. The corresponding four-level Hamiltonian, expressed in the basis $\{|S_1\uparrow_4\rangle, |D_{124}^{\prime(+1/2)}\rangle, |D_{124}^{(+1/2)}\rangle, |S_4\uparrow_1\rangle\}$, reads

$$\hat{H}_{\text{eff}} = \begin{pmatrix} E_1 & \tilde{\tau}_1 & 0 & \tilde{\tau}_2 \\ \tilde{\tau}_1 & E_2 & 0 & \tilde{\tau}_3 \\ 0 & 0 & E_3 & \tilde{\tau}_4 \\ \tilde{\tau}_2 & \tilde{\tau}_3 & \tilde{\tau}_4 & E_4 \end{pmatrix}. \tag{19}$$

Explicit expressions for the effective energies and hopping amplitudes are provided in the Supplementary Note 5. Using the chosen working parameters, we find that $|\tilde{\tau}_1| \gg |\tilde{\tau}_2|, |\tilde{\tau}_3|, |\tilde{\tau}_4|$. Diagonalizing the Hamiltonian reveals two pairs of eigenstates, in which $|S_1\uparrow_4\rangle$ and $|D_{124}^{\prime(+1/2)}\rangle$ weakly coupled to the remaining states. Since $|S_4\uparrow_1\rangle$ is the only state within the transport window, current is suppressed, and the system becomes trapped in the first pair of states, leading to current blockade. Nonetheless, a dephasing mechanism can induce leakage from the first pair of states to the second one enabling a finite current. In the central region of the crossing in Fig. 9a, the current flows via the sequence $|S_1\uparrow_4\rangle \to |D_{124}^{\prime(+1/2)}\rangle \to |D_{124}^{(+1/2)}\rangle \to |S_4\uparrow_1\rangle$. Although $|D_{124}^{\prime(+1/2)}\rangle$ and $|D_{124}^{(+1/2)}\rangle$ are not directly coupled in the effective Hamiltonian, dephasing enables transitions between them. This process is schematically illustrated in Fig. 9b. In the limit of vanishing dephasing

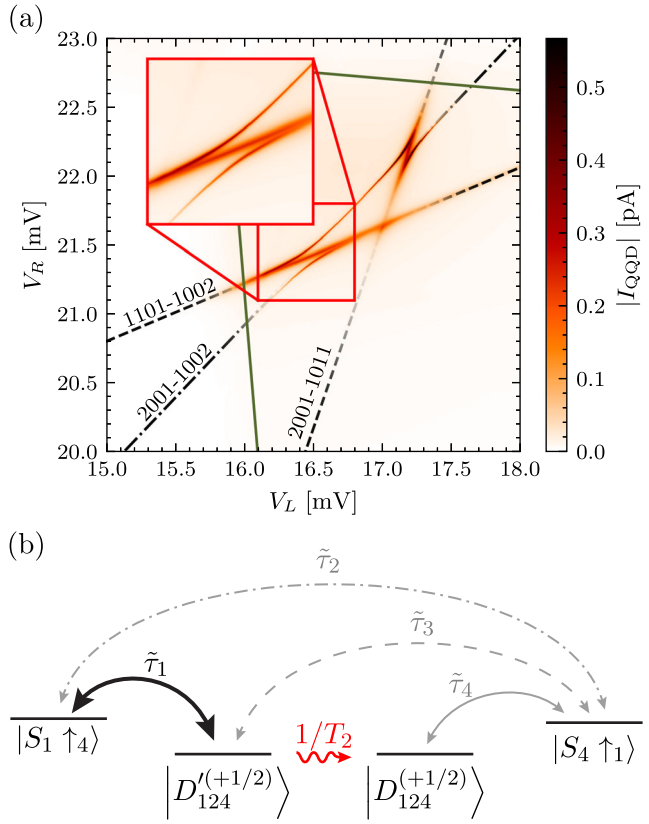

Fig. 9 | Current and energy diagram in the three-particle regime near the 2001–1002 resonance. a Current map as a function of the gate voltages applied to the left- and right-most dots, V_L and V_R, respectively. Dark green lines indicate the region of positive current. Black dashed and dot-dashed lines represent different resonance conditions, as labeled. The detuning of the center dots is $\varepsilon_{20} = \varepsilon_{30} = -367$ μeV, and $U_i = [1500, 1650, 1220, 1800]\,\mu$eV, $V_i = [1000, 500, 333]\,\mu$eV. A zoom-in on the crossing between the 2001–1002 and 1101–1002 resonances is shown denoted by a red square. **b** Schematic of the effective model for the 2001–1002–1101 resonance. Strong coupling is depicted with a thick black line, while weak couplings are represented with thin gray lines. A dephasing mechanism is represented by a red wavy line.

($T_2 \to \infty$), not shown here, the current in the central region of the anticrossing disappear.

During this section, we have found a zoo of different long-range transport processes. The parameter sets used across the simulations are chosen to highlight specific resonances and features, such as avoided crossings, blockades, or symmetry effects. While not exhaustive, they reflect typical experimental values and are robust under moderate variations. In the Supplementary Note 6, we present the resonance conditions for two general states, offering a unifying framework for the transport maps observed.

Conclusions

We have analyzed long-range transfer in a QQD array under conditions of reduced symmetry. First, we investigated the single-particle regime. Using experimentally feasible parameters, we found that direct transfer between the first and last dots remains observable even in the presence of decoherence. An avoided crossing in the charge current, arising between distinct long-range processes, serves as a clear signature of coherent interference. We derived an effective model that accurately captures the system's dynamics, and obtained a simple analytical expression for the resonance condition associated with long-range transfer.

We further explored how long-range transfer persists in an interacting system with two and three electrons in the QQD. In this regime, we analyzed the contributions of different spin sectors independently, finding visible long-range transfers in all cases. In the case of two electrons, we find a coherent spin blockade of the current, which survives even in the presence of dephasing. For three particles in the $s = 3/2$ sector, we demonstrated that long-range transfer remains possible even when the central dots are singly occupied, yielding results analogous to the single-particle case. For the $s = 1/2$ sector, we showed that the two distant doublet states, though degenerate in the absence of magnetic fields, can be distinguished through the influence of dephasing, which imprints a characteristic signature in the charge current.

Although our work is theoretical in nature, it is grounded in experimentally realistic parameters and device architectures. The phenomena we predict of coherent long-range transfer, interference between resonant channels, and current blockade effects are all accessible with present-day measurement techniques. We therefore expect our results to serve not only as a framework for understanding transport in extended quantum dot arrays, but also as a guide for future experiments aiming to harness coherent charge dynamics for scalable quantum technologies.

Data availability

All the data shown in the figures of this work can be reproduced using custom codes (see the Code availability statement).

Code availability

All the codes needed to reproduce the results presented in this work are available at[55]. The simulations are based on the Lindblad master equation, which is solved using the QuTiP 5.1.1 library[56].

Received: 9 June 2025; Accepted: 10 September 2025;
Published online: 22 October 2025

References

1. Taylor, J. M. et al. Fault-tolerant architecture for quantum computation using electrically controlled semiconductor spins. *Nat. Phys.* **1**, 177–183 (2005).
2. Burkard, G., Ladd, T. D., Pan, A., Nichol, J. M. & Petta, J. R. Semiconductor spin qubits. *Rev. Mod. Phys.* **95**, 025003 (2023).
3. De Franceschi, S. et al. Electron cotunneling in a semiconductor quantum dot. *Phys. Rev. Lett.* **86**, 878–881 (2001).
4. Shinkai, G., Hayashi, T., Ota, T., Muraki, K. & Fujisawa, T. Bidirectional current drag induced by two-electron cotunneling in coupled double quantum dots. *Appl. Phys. Express* **2**, 081101 (2009).
5. Weymann, I., Bułka, B. R. & Barnaś, J. Dark states in transport through triple quantum dots: the role of cotunneling. *Phys. Rev. B* **83**, 195302 (2011).
6. Braakman, F. R., Barthelemy, P., Reichl, C., Wegscheider, W. & Vandersypen, L. M. K. Long-distance coherent coupling in a quantum dot array. *Nat. Nanotechnol.* **8**, 432–437 (2013).
7. van der Wiel, W. G. et al. Electron transport through double quantum dots. *Rev. Mod. Phys.* **75**, 1–22 (2002).
8. Jouravlev, O. N. & Nazarov, Y. V. Electron transport in a double quantum dot governed by a nuclear magnetic field. *Phys. Rev. Lett.* **96**, 176804 (2006).
9. Busl, M. & Platero, G. Spin-polarized currents in double and triple quantum dots driven by ac magnetic fields. *Phys. Rev. B* **82**, 205304 (2010).
10. Wang, D. Q. et al. Anisotropic Pauli spin blockade of holes in a GaAs double quantum dot. *Nano Lett.* **16**, 7685–7689 (2016).
11. Dani, O., Hussein, R., Bayer, J. C., Kohler, S. & Haug, R. J. Temperature-dependent broadening of coherent current peaks in InAs double quantum dots. *Commun. Phys.* **5**, 292 (2022).
12. Fernández-Fernández, D., Picó-Cortés, J., Vela Liñán, S. & Platero, G. Photo-assisted spin transport in double quantum dots with spin-orbit interaction. *J. Phys.: Mater.* **6**, 034004 (2023).
13. Saraga, D. S. & Loss, D. Spin-entangled currents created by a triple quantum dot. *Phys. Rev. Lett.* **90**, 166803 (2003).

14. Gaudreau, L. et al. Stability diagram of a few-electron triple dot. *Phys. Rev. Lett.* **97**, 036807 (2006).
15. Michaelis, B., Emary, C. & Beenakker, C. W. J. All-electronic coherent population trapping in quantum dots. *Europhys. Lett.* **73**, 677–683 (2006).
16. Schröer, D. et al. Electrostatically defined serial triple quantum dot charged with few electrons. *Phys. Rev. B* **76**, 075306 (2007).
17. Rogge, M. C. & Haug, R. J. Two-path transport measurements on a triple quantum dot. *Phys. Rev. B* **77**, 193306 (2008).
18. Rogge, M. C. & Haug, R. J. The three dimensionality of triple quantum dot stability diagrams. *N. J. Phys.* **11**, 113037 (2009).
19. Granger, G. et al. Three-dimensional transport diagram of a triple quantum dot. *Phys. Rev. B* **82**, 075304 (2010).
20. Villavicencio, J., Maldonado, I., Cota, E. & Platero, G. Quasienergy spectrum and tunneling current in ac-driven triple quantum dot shuttles. *N. J. Phys.* **13**, 023032 (2011).
21. Gaudreau, L. et al. Coherent control of three-spin states in a triple quantum dot. *Nat. Phys.* **8**, 54–58 (2011).
22. Amaha, S. et al. Resonance-hybrid states in a triple quantum dot. *Phys. Rev. B* **85**, 081301 (2012).
23. Amaha, S. et al. Two- and three-electron Pauli spin blockade in series-coupled triple quantum dots. *Phys. Rev. Lett.* **110**, 016803 (2013).
24. Kotzian, M., Gallego-Marcos, F., Platero, G. & Haug, R. J. Channel blockade in a two-path triple-quantum-dot system. *Phys. Rev. B* **94**, 035442 (2016).
25. Wang, B.-C. et al. Photon-assisted tunneling in an asymmetrically coupled triple quantum dot. *J. Appl. Phys.* **120**, 064302 (2016).
26. Picó-Cortés, J., Gallego-Marcos, F. & Platero, G. Direct transfer of two-electron quantum states in ac-driven triple quantum dots. *Phys. Rev. B* **99**, 155421 (2019).
27. Hendrickx, N. W. et al. A single-hole spin qubit. *Nat. Commun.* **11**, 3478 (2020).
28. von Horstig, F.-E. et al. Electrical readout of spins in the absence of spin blockade. *arXiv* arXiv:2403.12888 (2024).
29. Busl, M. et al. Bipolar spin blockade and coherent state superpositions in a triple quantum dot. *Nat. Nanotechnol.* **8**, 261–265 (2013).
30. Sánchez, R. et al. Long-range spin transfer in triple quantum dots. *Phys. Rev. Lett.* **112**, 176803 (2014).
31. Sánchez, R., Gallego-Marcos, F. & Platero, G. Superexchange blockade in triple quantum dots. *Phys. Rev. B* **89**, 161402 (2014).
32. Haug, R., Hong, J. & Lee, K. Electron transport through one quantum dot and through a string of quantum dots. *Surf. Sci.* **263**, 415–418 (1992).
33. Thalineau, R. et al. A few-electron quadruple quantum dot in a closed loop. *Appl. Phys. Lett.* **101**, 103102 (2012).
34. Delbecq, M. R. et al. Full control of quadruple quantum dot circuit charge states in the single electron regime. *Appl. Phys. Lett.* **104**, 183111 (2014).
35. Fujita, T., Baart, T. A., Reichl, C., Wegscheider, W. & Vandersypen, L. M. K. Coherent shuttle of electron-spin states. *npj Quant. Inf.* **3**, 22 (2017).
36. Bayer, J. C., Wagner, T., Rugeramigabo, E. P. & Haug, R. J. Charge reconfiguration in arrays of quantum dots. *Phys. Rev. B* **96**, 235305 (2017).
37. Bayer, J. C., Wagner, T., Rugeramigabo, E. P. & Haug, R. J. Charge reconfiguration in isolated quantum dot arrays. *Ann. der Phys.* **531**, 1800393 (2019).
38. Ban, Y., Chen, X., Kohler, S. & Platero, G. Spin entangled state transfer in quantum dot arrays: coherent adiabatic and speed-up protocols. *Adv. Quantum Technol.* **2**, 1900048 (2019).
39. Kandel, Y. P. et al. Coherent spin-state transfer via Heisenberg exchange. *Nature* **573**, 553–557 (2019).
40. Mills, A. R. et al. Shuttling a single charge across a one-dimensional array of silicon quantum dots. *Nat. Commun.* **10**, 1063 (2019).
41. Liu, D. E., Chandrasekharan, S. & Baranger, H. U. Quantum phase transition and emergent symmetry in a quadruple quantum dot system. *Phys. Rev. Lett.* **105**, 256801 (2010).
42. von Stecher, J., Demler, E., Lukin, M. D. & Rey, A. M. Probing interaction-induced ferromagnetism in optical superlattices. *N. J. Phys.* **12**, 055009 (2010).
43. Creffield, C. E. & Platero, G. Dynamical control of correlated states in a square quantum dot. *Phys. Rev. B* **66**, 235303 (2002).
44. Vitanov, N. V., Rangelov, A. A., Shore, B. W. & Bergmann, K. Stimulated Raman adiabatic passage in physics, chemistry, and beyond. *Rev. Mod. Phys.* **89**, 015006 (2017).
45. Kalantre, S. S. et al. Machine learning techniques for state recognition and auto-tuning in quantum dots. *npj Quant. Inf.* **5**, 6 (2019).
46. Zwerver, A. M. J. et al. Qubits made by advanced semiconductor manufacturing. *Nat. Electron.* **5**, 184–190 (2022).
47. Losert, M. P. et al. Strategies for enhancing spin-shuttling fidelities in Si/Si Ge quantum wells with random-alloy disorder. *PRX Quantum* **5**, 040322 (2024).
48. David, A. et al. Long distance spin shuttling enabled by few-parameter velocity optimization. *arxiv* arXiv:2409.07600 (2024).
49. Busl, M., Sánchez, R. & Platero, G. Control of spin blockade by ac magnetic fields in triple quantum dots. *Phys. Rev. B* **81**, 121306 (2010).
50. Greentree, A. D., Cole, J. H., Hamilton, A. R. & Hollenberg, L. C. L. Coherent electronic transfer in quantum dot systems using adiabatic passage. *Phys. Rev. B* **70**, 235317 (2004).
51. Ban, Y., Chen, X. & Platero, G. Fast long-range charge transfer in quantum dot arrays. *Nanotechnology* **29**, 505201 (2018).
52. Fernández-Fernández, D., Ban, Y. & Platero, G. Flying spin qubits in quantum dot arrays driven by spin-orbit interaction. *Quantum* **8**, 1533 (2024).
53. Fallahi, S., Nakamura, J. R., Gardner, G. C., Yannell, M. M. & Manfra, M. J. Impact of silicon doping on low-frequency charge noise and conductance drift in GaAs/AlxGa1-xAs nanostructures. *Phys. Rev. Appl.* **9**, 034008 (2018).
54. Liang, S., Nakamura, J., Gardner, G. C. & Manfra, M. J. Reduction of charge noise in shallow GaAs/AlGaAs heterostructures with insulated gates. *Appl. Phys. Lett.* **117**, 133504 (2020).
55. Fernandez-Fernandez, D. Davtax/Long_range_QQD: v1.0 (2025). https://doi.org/10.5281/zenodo.16310123.
56. Lambert, N. et al. QuTiP 5: The Quantum Toolbox in Python (2024).

Acknowledgements

G.P. and D.F.F. are supported by the Spanish Ministry of Science through the grant PID2023-149072NB-I00, by the CSIC Research Platform PTI-001, and acknowledge the Severo Ochoa Centers of Excellence program through Grant CEX2024-001445-S. D.F.F. acknowledges support from FPU Program No. FPU20/04762. J.C.B and R.J.H are supported by the Deutsche Forschungsgemeinschaft (DFG, German Research Foundation) under Germany's Excellence Strategy - EXC 2123 QuantumFrontiers - 390837967 and the State of Lower Saxony of Germany via the Hannover School for Nanotechnology.

Author contributions

D.F.F. performed the numerical simulations and theoretical modelling. J.C.B. contributed to the discussions concerning the potential experimental implementation. All authors contributed to the interpretation of the results. D.F.F. wrote the first draft, and all authors contributed to the writing and revision of the final version. R.J.H. and G.P. supervised the project.

Competing interests

The authors declare no competing interests.

Additional information

Supplementary information The online version contains supplementary material available at https://doi.org/10.1038/s42005-025-02319-3.

Correspondence and requests for materials should be addressed to David Fernández-Fernández.

Peer review information : *Communications Physics* thanks John Nichol and the other, anonymous, reviewer(s) for their contribution to the peer review of this work. [A peer review file is available].